Vibrational Spectroscopy 75 (2014) 107–117

Contents lists available at ScienceDirect

Vibrational Spectroscopy

journal homepage: www.elsevier.com/locate/vibspec

Importance of weak interactions and conformational equilibrium in *N*-butyl-*N*-methylpiperidinium bis(trifluromethanesulfonyl) imide room temperature ionic liquids: Vibrational and theoretical studies

Madhulata Shukla [a], Hemanth Noothalapati [b], Shinsuke Shigeto [b], Satyen Saha [a,*]

[a] Department of Chemistry, Faculty of Science, Banaras Hindu University, Varanasi 221 005, India
[b] Department of Applied Chemistry and Institute of Molecular Science, National Chiao Tung University, Hsinchu 30010, Taiwan

ARTICLE INFO

Article history:
Received 10 May 2014
Received in revised form 19 September 2014
Accepted 25 October 2014
Available online 30 October 2014

Keywords:
Ionic liquid
Piperidinium cation
Bis(trifluoromethanesulfonyl)imide anion
Raman spectroscopy
Vibrational modes
H-bonding interaction
Interaction energy
Density functional theory

ABSTRACT

Piperidinium cation-based room temperature ionic liquids (RTILs) constitute an important class of ILs because of their unique electrochemical properties as well as non-aromatic nature of the cation. However, detailed structural studies are yet to be done. In this paper, we discuss the molecular structure and vibrational spectra of *N*-butyl-*N*-methylpiperidinium bis(trifluromethanesulfonyl) imide, ($PIP_{14}NTf_2$; where, PIP_{14} is *N*-butyl-*N*-methylpiperidinium and NTf_2 is bis(trifluromethanesulfonyl) imide), obtained with a combined approach of infrared (IR) and Raman spectroscopies in the liquid state and density functional theory (DFT) and Hartree–Fock (H–F) based theoretical calculations. DFT calculations, which are found to produce the most stable geometry compared to other two methods (MP2 and H–F), reproduce the experimental IR and Raman spectra reasonably well. Our findings reveal structural properties that profoundly influence intermolecular interactions and melting point. There exists a large variation in the melting point of the ILs studied. While the bromide salt of the piperidinium derivative ($PIP_{14}Br$) is solid with very high melting point (241 °C), the corresponding NTf_2 salt is low viscous liquid at room temperature (mp: −25 °C). bmimBr (bmim = 1-butyl-1-methylimidazolium) exhibits a substantially lower melting point of 79 °C than $PIP_{14}Br$, suggesting that more number of strong classical hydrogen bonding interactions in the latter is primarily responsible for the much higher melting point. In addition, involvement of the alkyl group in PIP_{14} in H-bonding interaction provides additional rigidity in *n*-butyl chain which is otherwise absent in bmimBr. Interaction energy for $PIP_{14}Br$ is found to be higher than $PIP_{14}NTf_2$, showing a positive correlation between interaction energy and melting point. A blue shift in C—H stretching wavenumber as evident from IR and Raman spectra of $PIP_{14}Br$ IL is a clear indication of the stronger hydrogen bonding as compared to $PIP_{14}NTf_2$ IL. Furthermore, we experimentally observe the existence of *cis*oid–*trans*oid conformational equilibrium of NTf_2^- anion in the Raman spectrum of $PIP_{14}NTf_2$ for the first time and determined that *trans*oid NTf_2^- anion to be more stable than the corresponding *cis*oid conformer by 1.04 kcal/mol using DFT. Examination of various conformational possibilities of the cation shows that the butyl group preferentially exists in *gauche* conformation.

1. Introduction

In recent years, ionic liquids (ILs) have become a rapidly expanding topic of chemical research on account of their unique properties that include a negligible vapor pressure, nonflammability and good ability to dissolve organic and inorganic compounds, and even polymeric materials [1,2]. These unusual properties mean that ILs are superior media for a broad range of potential uses, such as environmentally friendly solvent for chemical synthesis or biocatalysis. They are also used in electrochemical devices and processes, such as rechargeable lithium batteries and electrochemical capacitors, etc. Rechargeable lithium batteries are a ubiquitous energy device that is being worldwide in many types of portable electronic equipment, such as cellular phones, laptop computers, and digital cameras. Cyclic alkyl quaternary ammonium (QA) based cations, *N*-alkyl-*N*-methylpiperidinium (PIP_{1n}; where, *n* indicates the number of carbon atoms in the linear alkyl chain) are a class of cations whose room temperature ILs (RTILs) are very promising in the field of electrochemical applications due to their high thermal and

* Corresponding author. Tel.: +91 9935913366; fax: +91 542 2368127.
E-mail address: ssahabhu@yahoo.com (S. Saha).

http://dx.doi.org/10.1016/j.vibspec.2014.10.006
0924-2031/

electrochemical stabilities [3–18]. As an example, $PIP_{1n}NTf_2$; where, NTf_2 stands for bis(trifluoromethanesulfonyl) imide, is recently proposed for high-voltage supercapacitors and lithium batteries [10–13]. Electrochemical stability is one of the reasons for recent growing interest in QA based ILs in addition to the low cathodic potentials of the QA cations compared to 1,3-dialkylimidazolium cations. Because of the wide electrochemical windows, these ILs are used as solvent-free supporting electrolytes in electrochemical devices and also increase their safety.

As the properties of any material depend on the structure of molecules in different phases, it is very important to understand the structural features of ILs in depth. The ubiquitous properties of ILs are governed by the type and strength of interaction between their constituents [19–21]. Recently, the possibilities of existence of ordered local structure, i.e., microheterogeneity in ionic liquids have got considerable attentions [22–25]. In general, liquids are much less understood than gases and crystals. Structure in the gas phase can be accurately determined by electron diffraction or high-resolution rotationally-resolved spectroscopy, and solid/crystal structure can be determined by X-ray and/or neutron diffraction. In contrast, the diffraction techniques have limited applicability to elucidate liquid structure. Understanding the microscopic interactions at the molecular level is indeed a challenge in particular for ILs. While vast amount of studies have been made on imidazolium based ILs, very few literatures are available related to structural and vibrational studies on these useful PIP_{1n}-based ILs. Here we report a detailed structural study of PIP_{14}-based ILs using density functional theory (DFT) calculations and vibrational spectroscopy (both IR and Raman). Theoretical calculations, in particular DFT, are of very much importance in predicting the structure of different RTILs [26,27]. DFT calculation also helps us to understand the interaction present among cation and anion in the molecule as well as the type of bonding present in the molecule. The DFT calculated vibrational spectra gives us a strong base to analyze the experimental spectra (both IR and Raman) including the effect of interaction causing shifting in Raman/IR bands [28].

Among various physical properties, melting point is the most important for ILs. This property is determined by the strength of its crystal lattice packing, which is in turn controlled by three main factors: (i) molecular symmetry, (ii) intermolecular interactions, and (iii) conformational degrees of freedom of the molecule. According to Fumino and Ludwig [29], although ILs consists solely of cations and anions and Coulomb forces are the dominating interaction, a local and directional interaction such as hydrogen bonding has significant influence on the structure and properties of ionic liquids. It has also been explained by Kempter et al. [30] that in ILs, hydrogen bonding is the major interaction which control the physical properties of ILs. Strength of H-bonding can be well studied by the vibrational spectroscopy [26,29]. As the interaction strength increases between cation and anion, vibrational frequencies shift to higher wavenumber due to increasing force constants indicating stronger interaction between the ion species [29]. A shift in the wavenumber of intermolecular vibrational bands can be correlated to the change in force constants or reduced masses of anion. Larger and heavier anions interact weakly with the cation, whereas, smaller and lighter anions provide strong interaction potential due to their higher surface charge density. Thus, both parameters; the reduced mass as well as the force constant, lead to shift into the same direction, namely to lower or higher frequencies, respectively. This statement has been well justified by our previous publication [26].

In this paper we choose two sets of ionic salts: (1) $PIP_{14}Br$ and 1-butyl-3-methylimidazolium bromide (bmimBr) (anion same) and (2) $PIP_{14}Br$ and $PIP_{14}NTf_2$ (cation same) with an aim to pinpoint the major interaction which determines the physical state of a salt. Except the very recent publication by Siqueira et al. [31] where they have studied *N*,*N*-butyl-methylpiperidinium, in combination with 1-ethyl-3-methylimidazolium, 1-butyl-3-methylimidazolium and 1-butyl-2,3-dimethylimidazolium cations based ILs and evaluated the effects of chain length, ability of developing hydrogen bond, electronic delocalization of their positively charged region, no other vibrational studies can be found on piperidinium ionic liquid despite their significant importance. They have made the structural studies of all these cations through XRD and DFT studies as well as vibrational studies using Raman spectroscopy. Also they have investigated that very similar local environment is experienced by all these organic cations in the interlayer space and in ionic liquids with NTf_2 anion [31]. This study reveals that it is indeed the H-bonding interaction along with conformational variety of constituents that largely controls the physical state of the salt. We establish that $PIP_{14}Br$ is a colorless solid and more than one interaction is present between cation and anion. This fact contrasts with bmimBr, where only one interaction is present between cation and anion and is found to exist as low melting solid (mp: ~79 °C). Further, Raman and DFT studies show that NTf_2^- anion found to exist in *cis*oid–*trans*oid conformational equilibrium in $PIP_{14}NTf_2$ IL analogous to *n*-butyl chain in imidazolium cation. We also present studies of non-ionic species of corresponding ionic constituents to understand the stabilization due to formation of ionic liquids. To our best of knowledge, this is the first report on the vibrational–theoretical studies of interactions for piperidinium cationic ionic liquids.

2. Methodology

2.1. Reagents and instrumentation

N-Methylpiperidine (Sigma–Aldrich, redistilled, >99%), bromobutane (Merck, Germany), bis(trifluoromethanesulfonyl) imide (Sigma–Aldrich, redistilled, >99%) were used as received for the synthesis. Acetonitrile (HPLC grade), ethyl acetate (EtOAc, HPLC grade) were procured from Merck, Germany and were used after purification following standard procedures. IR spectra of $PIP_{14}Br$ and $PIP_{14}NTf_2$ were measured with Varian FTIR 3100 in the region 400–3500 cm^{-1} using neat samples. 300 MHz NMR (JEOL) was used to measure the ^1H NMR. Raman spectra were measured with a home-made Raman microspectrometer setup with CW 633 nm (He–Ne) excitation. Details of the experimental setup were described elsewhere [32]. Raman spectra were obtained with low laser power (~1.2 mW) with 10 s exposure. The Raman spectra presented here are after background correction.

2.2. Synthesis of N-*methyl*-N-*butylpiperidinium bromide* ($PIP_{14}Br$)

A general synthesis procedure for synthesizing $PIP_{14}Br$ was reported in literature [6,14]. A modified form of the reported procedure was followed: instead of using high temperature, lower temperature was used with a longer time of stirring. This excludes major possibilities of inclusion of impurities in resultant ILs. The scheme for the synthesis of $PIP_{14}Br$ is shown in Fig. 1. 20 mL of ethyl acetate was taken in 100 mL round bottom (RB) flask. *N*-Methyl piperidine (8.0 g, 82 mmol) was added to it with stirring and then bromobutane (12.0 g, 90 mmol) was added slowly with continuous stirring at 20 °C in nitrogen atmosphere. The mixture was stirred for 16 h at 30 °C followed by stirring at 50 °C for 3 h. The reaction mixture was then washed with 150 mL dry distilled EtOAc. The solvent was then evaporated on a rotavapour under reduced pressure to get white solid powder, which was further kept under high vacuum at 50 °C for 3 h (yield: 90%). Melting point (mp) of the salt was found to be 241 °C and therefore is not an IL according to standard definition. The product was confirmed by ^1H NMR (δ, ppm, 1.01 (t, 3H), 1.47 (q, 2H), 1.72 (8H), 3.63 (s, 3H), 3.66 (4H), 3.81

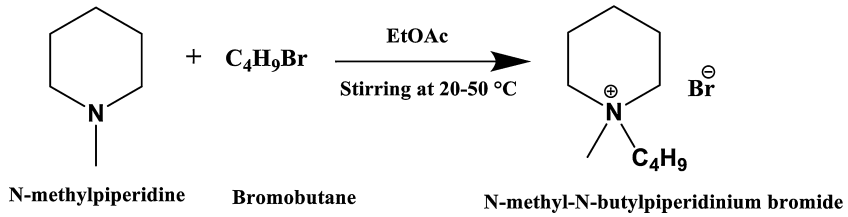

Fig. 1. Scheme for the synthesis of *N*-methyl-*N*-butylpiperidinium bromide, ($PIP_{14}Br$).

(2H)); and by IR (569, 673, 904, 940, 1030, 1227, 1369, 1464, 2874, 2959 cm^{-1}).

2.3. Synthesis of N-methyl-N-butylpiperidinium bis (trifluoromethanesulfonyl) imide ($PIP_{14}NTf_2$)

$PIP_{14}Br$ was taken as a precursor for the synthesis of $PIP_{14}NTf_2$. The scheme for preparation of $PIP_{14}NTf_2$ is shown in Fig. 2. $PIP_{14}Br$ (4.5 g, 20 mmol) was taken in a RB flask containing 10 mL of triple distilled (TD) water. $LiNTf_2$ (6.0 g, 21 mmol) dissolved in 10 mL TD water was added to it at 35 °C and stirring was continued for 4 h. 150 mL dichloromethane (DCM) was used to extract the product, which was repeatedly washed with cold TD water to remove any ionic impurity. DCM was then evaporated on a vacuum rotavapour and kept under high vacuum for 2 h at 50 °C. Light yellow liquid was obtained (yield: 88%). Relatively higher temperature (~80 °C) provides more yield [6,14] but was found to produce darker yellow colored liquid. The light yellow colored liquid was further dissolved in 10 mL of pure acetonitrile (ACN) to treat with activated charcoal for decolorization. The mixture was stirred for 4 h followed by filtration through a sintered column packed with fresh charcoal and activated alumina. The resultant solution was evaporated on rotavapour at reduced pressure to get a completely colorless liquid product. The product was confirmed as desired ionic liquid by ^1H NMR (δ, ppm, 1.01 (t, 3H), 1.44 (q, 2H), 1.74 (8H), 3.42 (s, 3H), 3.56 (4H), 3.85 (2H)); and by IR (570, 619, 1054, 1139, 1197, 1348, 1474, 2881, 2966 cm^{-1}).

2.4. Computational details

Quantum chemical calculations were used for geometry optimization and vibrational frequencies calculation on cation, anion and ion pairs using Gaussian 03 package [33]. Geometry optimization was performed using density functional theory (DFT) [34], second Møller–Plesset (M–P2) and Hartree–Fock (H–F) methods to examine the most stable structure. DFT computations were performed at Becke's three-parameter hybrid model using Lee–Yang–Parr correlation functional (B–3L–Y–P) level of theory [35,36]. 6–31++G(d,p) basis set was used to obtain the optimized geometry and calculated IR and Raman frequencies. Two other popular methods, MP2 and H–F, were examined for better predictions of experimental IR and Raman frequencies [37]. No imaginary vibrational frequencies were obtained for the calculation reported here, indicating that the geometries of the ions were at the minimum of the potential surface. Correlation between experimental and calculated vibrational frequencies was established based on the literature values of similar derivatives by investigating the calculated frequencies through GaussView 5.0 software [38] and matching both the calculated frequencies and Raman activities with experiment. Since the Raman activities obtained from Gaussian calculations cannot be compared directly to the experimental Raman intensity [39–41], recently published methodology [42] was employed to convert the DFT calculated Raman activities to DFT calculated Raman intensity. Calculated Raman spectra are thus compared directly with the experimental Raman spectra and presented in various figures.

3. Results and discussion

3.1. Geometry optimization of cation and anion

Primarily the structure of cation and anion is optimized independently at the B–3L–Y–P/6–31++G(d,p) level of theory. The piperidine ring is found to be most stable in chair conformation when compared with other possible conformations such as boat or twist boat forms. This led us to use chair conformation as the initial input for the optimization of PIP cation as well as PIP based ILs. According to Siqueira et al. [31] also the most stable conformation of piperidine ring is the chair conformation like cyclohexane. The *n*-butyl chain attached to piperidinium cation is kept in *gauche* form, which is found to be more stable than *cis* and *trans* forms [17]. An energy level diagram for optimized piperidine (unsubstituted neutral molecule), *N*-methyl piperidine (substituted neutral molecule), *N*-methyl-*N*-butylpiperidinium cation (PIP_{14}^+), $PIP_{14}Br$ (salt), and $PIP_{14}NTf_2$ is depicted in Fig. 3. As expected, neutral or cationic species have higher energies than the ion pairs and perhaps illustrate the reason for the formation of ionic salt from constituents.

A survey of the literature related to the conformation of NTf_2^- reveals that both *cis*oid and *trans*oid conformations are possible [43–51]. While *cis*oid conformation has been proposed by Arnaud et al. [48] based on ab initio calculation on $LiNTf_2$, Johansson et al. [49] and Lopes and Padua [50] have reported *trans*oid as a more stable conformer. On the other hand, in crystalline state, *trans*oid

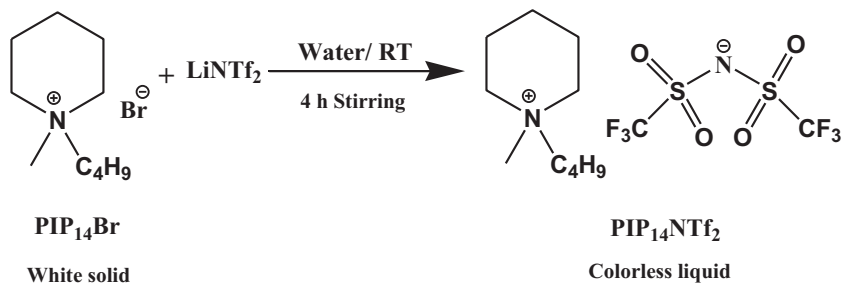

Fig. 2. Scheme for the synthesis of *N*-methyl-*N*-butylpiperidinium bis(trifluoromethanesulfonyl) imide ($PIP_{14}NTf_2$).

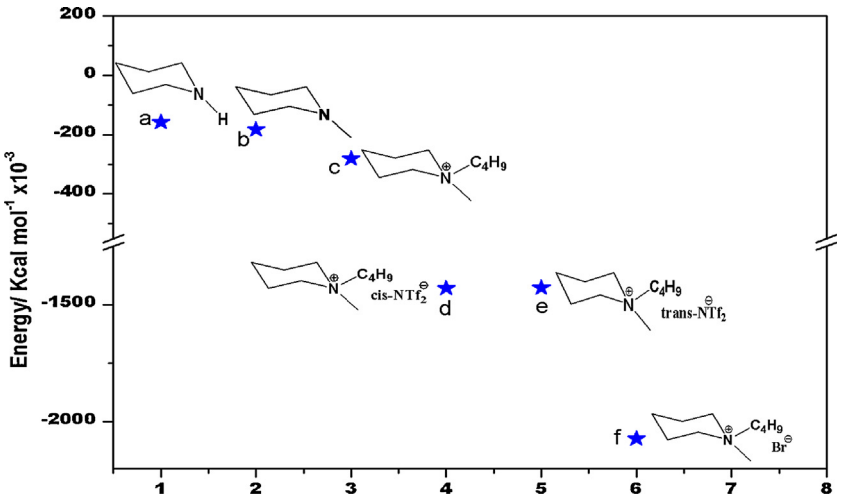

Fig. 3. DFT-calculated energies for optimized molecules of the neutral and charged constituents and the salts: (a) piperidine, (b) *N*-methylpiperidine, (c) *N*-methyl-*N*-butylpiperidinium cation (PIP_{14}^{+}), (d) *cis*-$PIP_{14}NTf_2$, (e) *trans*-$PIP_{14}NTf_2$, and (f) $PIP_{14}Br$. Calculated dipole moments are found to be 0.892, 0.466, 3.288, 16.787, 16.816, and 13.994 Debye for (a)–(f), respectively.

NTf_2^- was observed by Forsyth et al. [51]. It is plausible that while NTf_2^- is present predominantly in *trans*oid form, *cis*oid form can also be present as minor species. Recently, Faria et al. [52] in an impressive article have pointed out through Raman spectroscopic studies that, during crystallization of butyltrimethylammonium NTf_2^- IL, slow cooling process led to formation of *cis*oid NTf_2, whereas, fast cooling process led to formation of transoid NTf_2. Similar interesting observations are also reported for butylimidazolium NTf_2 (hbimNTf$_2$) derivative by Moschovi et al. [53]. According to them, in crystalline phase (i.e., at low temperature), NTf_2 adopts *trans* conformation, while upon melting, both conformations remains in equilibrium (enthalpy of the equilibrium ~8.5 kJ/mol). Interestingly, at elevated temperatures, NTf_2 predominantly remains in *cis* conformation. This variety of conformations of NTf_2 anion makes ILs comprising NTf_2^- an interesting topic of study. Hence, it is important to know which conformation of NTf_2^- does exist predominantly in the $PIP_{14}NTf_2$. DFT calculated dipole moment values for the *cis*oid and *trans*oid conformers are found to be quite different, 4.12 and 0.05 D, respectively. These dipole moment values closely match with those reported by Fujii et al. [43]. The significantly larger value for *cis*oid plausibly implies that when the counter ion (cation) is small, the *cis*oid geometry is preferred due to dipole–dipole interactions. Since, in the present study, the cation is reasonably large (compared to Li^+, etc.), it is expected that *trans*oid conformation is predominant. Our DFT calculation further indicated that the *trans*oid form (−1146638.63 kcal/mol) of the anion is more stable than the corresponding *cis*oid (−1146637.59 kcal/mol) by 1.04 kcal/mol (Fig. 4). These pieces of evidence led us to perform all the calculations on NTf_2^- anion based ILs with the *trans*oid conformation.

3.2. Geometry optimization of cation–anion ion pair

Based on the information obtained from the individual cation and anion species, the input structure of $PIP_{14}Br$ and $PIP_{14}NTf_2$ ion pairs are determined. While the chair form of piperidinium is taken for cation, the *trans*oid form of NTf_2^- anion is considered for the construction of $PIP_{14}NTf_2$ ion pair for calculations. Fig. 5 depicts the optimized molecular geometry of $PIP_{14}Br$ obtained at DFT/B–3L–Y–P/6–31++G(d,p) level calculation in gas phase. The important calculated parameters are tabulated in Table 1. The N—C and C—C bond lengths are found to be in the 1.51–1.54 Å range, which indicates single bond lengths. The C7—N1—C8 and N1—C8—C9 bond angles are found to be 110 and 116°, respectively, which deviate from the tetragonal geometry (109°) insignificantly. The N—C8—C9—C10 torsional angle is observed to be 163°, which deviate by just 2° from that reported by Reichert et al. for the crystal structural of $PIP_{14}I$ [17]. This explains that the butyl group is in *gauche* conformation similar to that in $PIP_{14}I$. The C8—C9—C10—C11 torsional angle is calculated to be 178°, indicating the *trans* form of the butyl chain. With respect to interactions present in the salt, Fig. 5 shows that the single bromide ion is involved in three hydrogen bonds (2.45, 2.54, and 2.57 Å) with the hydrogens of the cation. This indicates the presence of a strong interaction between monoatomic bromide anion and the cation. This perhaps leads to tight fitting of the ions in the crystal lattice and hence, to a high melting point of $PIP_{14}Br$ (i.e., 241 °C).

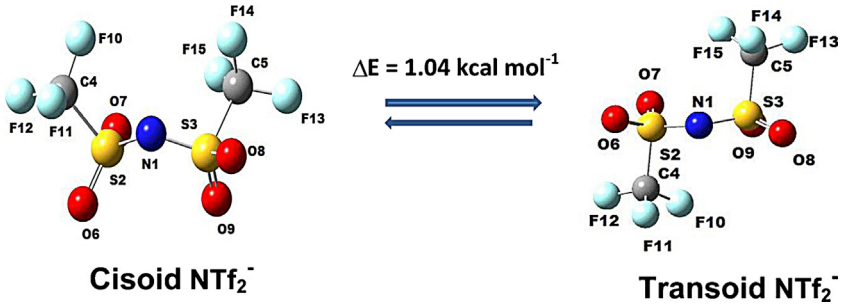

Fig. 4. *Cis*oid and *trans*oid conformations of NTf_2 anion. The terminal CF_3 rotates along the S—N bond to give rotational isomers. The twist angle (C4—S2—S3—C5) for *cis*oid is found to be −71°, while that for *trans*oid is 172°. The enthalpy difference was found to be 1.04 kcal/mol.

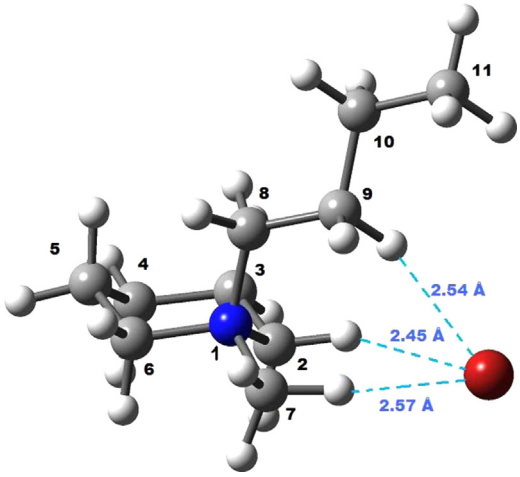

Fig. 5. DFT optimized structure of *N*-butyl-*N*-methylpiperidinium bromide, ($PIP_{14}Br$). The distances within the sum of van der Waals radii are also shown.

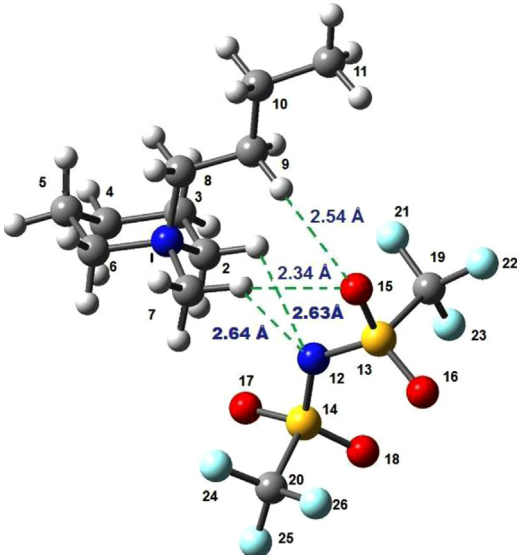

Fig. 6. DFT optimized structure of *N*-butyl-*N*-methylpiperidinium bis(trifluoromethanesulfonyl) imide, ($PIP_{14}NTf_2$). The distances within the sum of van der Waals radii are also shown.

Molecular geometry optimization of $PIP_{14}NTf_2$ ion pair was carried out using three different methods: DFT/B3–L–Y–P, MP2, and H–F, with an aim to find out the best method for this category of ILs. The important bond lengths, bond angles, torsional angles, and hydrogen bonding parameters are tabulated in Table 1. While bond length and bond angle parameters for piperidinium cation are found to be similar to those for $PIP_{14}Br$, the N1—C8—C9—C10 torsional angles are found to be 178°, 177°, and 171° from DFT, MP2, and H–F calculations respectively, which are different from 163° observed for $PIP_{14}Br$. This indicates that the butyl group in $PIP_{14}NTf_2$ ion pair exists in *trans* configuration. The C8—C9—C10—C11 torsional angle is observed to be 179° from DFT and MP2 calculation, indicating its *trans* conformation around the C9—C10 bond. An excellent correlation is also observed between experimental and calculated geometric parameters of NTf_2^- anion. For e.g., N—S, S=O, S—C, and C—F bond lengths calculated using DFT show very minor deviation (0.05, 0.04, 0.07, and 0.01 Å, respectively) from the reported crystal data [43]. Though bond lengths calculated by H–F method are in better agreement with crystals data, its bond angle and torsional angles predictions are grossly different (vide Table 1). On the other hand, B–3L–Y–P level of theory fairly well reproduce bond angles and torsional angles (e.g., see S—N—S bond angle, C—S—S—C, and S—N—S—C torsional angles in Table 1). MP2 calculation also produces similar results as DFT, but it consumed nearly three times computational time compared to that of DFT calculation. Therefore, it appears from our studies, that DFT is most reasonable for geometry optimization studies of piperidinium based salts. Classical hydrogen bonding interaction present between cation and anion are shown in Fig. 6 as broken lines. C7—H—N12, C7—H—O15, C9—H—O15, and C2—H—N12 hydrogen bonds are found to have bond lengths of 2.64, 2.34, 2.54, and 2.63 Å, respectively. Among the two salts examined, $PIP_{14}Br$ was found to be more stable than $PIP_{14}NTf_2$ by 590 kcal/mol (Fig. 3). Both the possible structures of $PIP_{14}NTf_2$ having the *cis*oid or *trans*oid form of NTf_2^- anion have also been studied theoretically and *trans*oid-$PIP_{14}NTf_2$ is found to have a slightly lower energy (by 0.38 kcal/mol) compared to *cis*oid-$PIP_{14}NTf_2$ (see Fig. 3).

3.3. Hydrogen bonding interaction and interaction energies

Studies of hydrogen bonding interaction present in ILs are important as the number of H-bond donors, the interaction strength, and the type of network formation can be tailored to get a

Table 1
Selected bond lengths (Å), bond angles (°) and dihedral angles (°) for optimized structure of $PIP_{14}Br$ using DFT method and $PIP_{14}NTf_2$ using DFT, MP2, and H–F methods as well as its reported crystal data.

Parameter	$PIP_{14}Br$	Parameter/$PIP_{14}NTf_2$	Crystal data of NTf_2 anion [25]	DFT results	MP2 results	H–F results
N1—C2	1.52 Å	Anion				
N1—C7	1.51 Å	N12—S14	1.57 Å	1.62 Å	1.62 Å	1.57 Å
N1—C6	1.53 Å	S14—O17	1.42 Å	1.46 Å	1.46 Å	1.42 Å
C2—C3	1.54 Å	S14—C20	1.83 Å	1.89 Å	1.88 Å	1.83 Å
C2—H—Br	2.45 Å	C20—F24	1.32 Å	1.33 Å	1.34 Å	1.32 Å
C7—H—Br	2.57 Å	S13—N12—S14	125°	126°	124°	129°
C9—H—Br	2.54 Å	S13—N12—S14—C20	92°	89°	101°	103°
C2—H—Br	153°	S14—N12—S13—C19	92°	89°	93°	89°
C7—H—Br	155°	C20—S14—S13—C19	172°	165°	171°	161°
C9—H—Br	156°	Cation				
C7—N1—C8	110°	C7—N1—C8	–	109°	109°	109°
N1—C8—C9	116°	N1—C8—C9	–	116°	115°	116°
N—C8—C9—C10	163°	N—C8—C9—C10	–	178°	177°	171°
C8—C9—C10—C11	176°	C8—C9—C10—C11	–	179°	179°	177°
		Cation–anion interaction				
		C7—H—N12	–	2.64 Å	2.57 Å	2.70 Å
		C7—H—O15	–	2.34 Å	2.32 Å	2.42 Å
		C9—H—O15	–	2.54 Å	2.29 Å	2.69 Å
		C2—H—N12	–	2.63 Å	2.38 Å	2.72 Å

variety of ILs [28]. In this study, we have chosen a particular cation with two distinctly different anions having quite different size, flexibility, interacting sites, and H-bonding formation capability. These two anions, Br^- and NTf_2^-, on the other hand, represent two extreme cases in the sense that while the former is a single atom based anion, the latter is a multidentate, conformationally flexible, considerably larger anion. The difference in hydrogen bonding pattern is presented in Figs. 5 and 6. There are three H-bonding interactions found in $PIP_{14}Br$ with H—Br distances 2.57, 2.45, and 2.54 Å, which are smaller than the sum of van der Waal radius of H and Br (3.05 Å) [54]. The corresponding angles C7—H—Br, C2—H—Br, and C9—H—Br were found to be 155°, 153°, and 156° respectively, indicating relatively stronger H-bonding interactions. It is worth mentioning that when compared with imidazolium analogue bmimBr, the melting point of $PIP_{14}Br$ is recorded to be higher by 162 °C (bmimBr mp = 79 °C, $PIP_{14}Br$ mp = 241 °C) [55]. The cations are different in the sense that imidazolium cation is aromatic in nature, whereas, piperidinium cation is a non-aromatic, quaternary ammonium salt. Interestingly, even though there is an additional possibility of having π–π interaction in imidazolium ILs in contrast to piperidinium cation based ILs, the melting point of the former is found to be much lower than the latter. Since the substituents are same (in both cases, butyl and methyl groups), it can fairly be assumed that there is no drastic change in hydrophobic interaction [56]. A close look at other interactions between cation and anion provides interesting differences. While in bmimBr, only one strong H-bonding interaction was observed between cation and anion involving C2—H—Br with a distance of 2.19 Å and angle of 154° [26,56], there are three H-bonding interactions present between cation and anion in $PIP_{14}Br$ (see Fig. 5). The H-bonding in the former involving most acidic C2—H is quite well known and extensively studied [56,57]. The single H-bond in bmimBr is, however, found to be quite stronger than any of the three individual H-bonding interactions present in $PIP_{14}Br$. The H-bonding interactions in $PIP_{14}Br$ are quite unique compared to corresponding imidazolium derivatives. In case of $PIP_{14}Br$, the Br^- anion holds all three segments (i.e., methyl group, *n*-butyl chain and piperidinium moiety) of PIP_{14} cation through H-bonding interactions, giving it more compact, less flexible cation–anion pair than corresponding bmimBr (see Fig. 5). This tempted us to infer that more number of H-bonding though weaker are more significant in determining the physical state than a stronger classical H-bonding interaction. Interestingly, when the anion in $PIP_{14}Br$ (having mp 241 °C) is changed by NTf_2 anion, the salt becomes a colorless, less viscous, RTIL (mp −25 °C).

The DFT optimized structure of $PIP_{14}NTf_2$ (Fig. 6) shows four H-bonding present between cation and anion; two are with the methyl group, one with the piperidinium ring, and one with the *n*-butyl chain. Although the number of H-bonding is larger in $PIP_{14}NTf_2$ (through multi-interacting sites), the melting point of $PIP_{14}Br$ is significantly higher than $PIP_{14}NTf_2$. Hence, the flexibility and volume of anion in this case appear to be more important than H-bonding interactions [58,59]. This finding has made us study the interaction between the cation and anion in more detail. The interaction energy (ΔE) is defined as the difference between the energy of the cation–anion pair (E_{AX}) and the sum of the energies of the isolated cationic (E_{A+}) and anionic (E_{X-}) species. The energies of the cation, anion and cation–anion pair of $PIP_{14}NTf_2$ are calculated using DFT, MP2, and H–F methods and are presented in Table 2. It is evident that the most stable geometry can be obtained from DFT calculation compared with MP2 (by 7 kcal/mol) and H–F (by 14 kcal/mol) method. It has been pointed out in our earlier report that interaction energy can provide us a fairly well indication of melting point of the salt [26]. The linear relationship between the melting points and the interaction energies ΔE has also been demonstrated very recently by Li et al. [60]. The interaction energy calculated for $PIP_{14}Br$ was found to be 90 kcal/mol, while that for $PIP_{14}NTf_2$ was observed to be only 70 kcal/mol, clearly showing the linear relationship between the melting points and interaction energy.

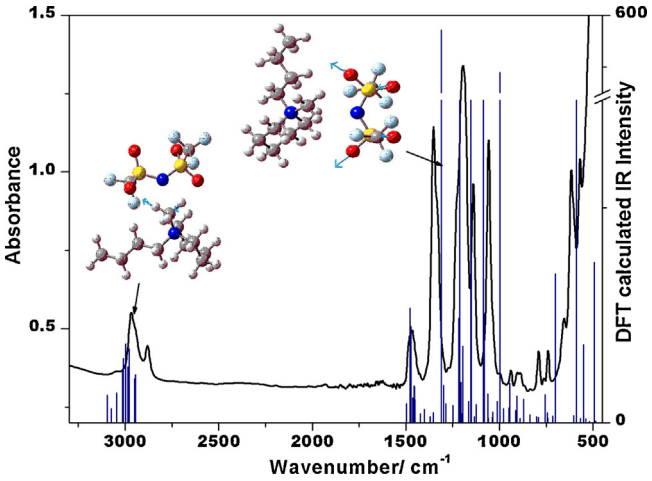

Fig. 7. IR spectrum of neat $PIP_{14}NTf_2$ (continuous line) and DFT calculated vibrational bands (vertical lines). A scaling factor of 0.966 was required to reproduce the experimental observations at the higher wavenumber region.

3.4. Understanding the interactions through vibrational spectral features for $PIP_{14}NTf_2$

Vibrational spectroscopy is a powerful tool to get the structural features and interactions present in ILs regardless of their physical states. Fumino and Ludwig [29] have demonstrated that far infrared (FIR) spectroscopy can be a suitable method for studying the cation–anion interaction in ionic liquids. Significant difference in wavenumber as well as intensity of the peak on variation of systematic variation of anion with imidazolium cation helped them to understand specific anion–cation interaction. Their experimental results supported by DFT calculation also indicates linear relationship between stretching frequency and binding energy. Since we have shown above that DFT can reproduce well the experimentally obtained structure and interactions, it is used to understand and explain the experimental IR and Raman spectra of synthesized $PIP_{14}NTf_2$. Fig. 7 shows the IR spectrum of $PIP_{14}NTf_2$

Table 2
Energies of PIP_{14}^+ cation, NTf_2^- anion and its ion pair, calculated using DFT, MP2, and H–F methods.

Methods	Energy of cation/kcal/mol x 10^3	Energy of anion/kcal/mol x 10^3	Total energy (cation + anion)/kcal/mol x 10^3 (I)	Energy of ion pair/kcal/mol x 10^3 (II)	Interaction energy kcal/mol (II–I)
DFT	−281.683	−1146.638	−1428.320	−1428.390	−70
MP2	−280.753	−1144.398	−1425.151	−1425.214	−63
H–F	−279.729	−1142.838	−1422.567	−1422.623	−56

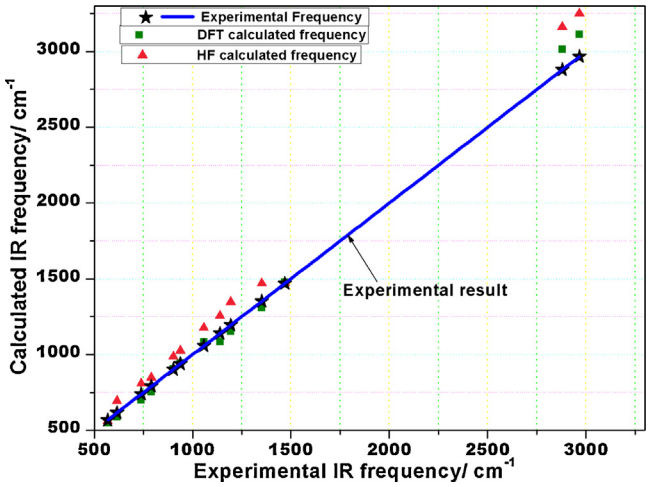

Fig. 8. Correlation diagram of experimental IR frequencies with DFT and H–F calculated frequencies for $PIP_{14}NTf_2$.

along with DFT calculated IR-active normal modes. The experimental IR spectrum shows major peaks at 570, 619, 1054, 1139, 1197, 1348, 1474, 2881, and 2966 cm^{-1}. To assign these peaks, both DFT/B–3L–Y–P and H–F calculation methods were used for $PIP_{14}NTf_2$ ion pair. The efficiency of DFT was clearly found to be better in reproducing the experimental results than that of H–F method. It can be seen from Fig. 8 that H–F method requires a significantly larger correction factor as compared to DFT in the higher wavenumber region. Similar indications have also been reported for a wide range of molecules [37,46]. On the basis of DFT calculation, experimental peaks have tentatively been assigned and are presented in Table 3. While the bands at 570 and 1054 cm^{-1} are assigned to the O=S=O scissoring, and S=O symmetric stretching (weakly coupled with S—N asymmetric stretching, respectively), the 1139 and 1197 cm^{-1} peaks correspond to C—F stretching and symmetric bendings, respectively. The bands at 2881 and 2966 cm^{-1} correspond to the symmetric and asymmetric C—H stretching modes of the cation. The IR frequencies derived from the DFT/B–3L–Y–P calculations agree reasonably well with the experimental frequencies (see Fig. 8). In addition, theoretically determined relative intensities are also found to be in good agreement with experimental IR intensities. The correlated

Table 3
Selected IR frequencies of $PIP_{14}NTf_2$ calculated using DFT and H–F methods.

Observed ν (cm^{-1})	DFT ν (cm^{-1})	H–F ν (cm^{-1})	Band assignment in $PIP_{14}NTf_2$
568	549	629	Scissoring in O=S=O and CF3
570	589	694	op bending of N and Scissoring in O=S=O
739	701	810	N—S sym stretching
790	755	847	C—F and N—S sym stretching
905	905	987	N—C(CH3) stretching and twisting in H—C—H
938	945	1025	Rocking of H—C—H, predominantly of piperidine ring CH2
1054	1086	1257	S=O sym stretching weakly coupled with S—N asym stretching
1139	1152	1346	C—F stretching
1197	1196	1379	C—F sym bending
1469	1480	1569	H—C—H wagging and umbrella bending in CH_3 group
2881	3015	3162	sym C—H stretching in Bu group
2966	3089	3241	asym C—H stretching in piperidinium ring

Sym–symmetric; asym–asymmetric.

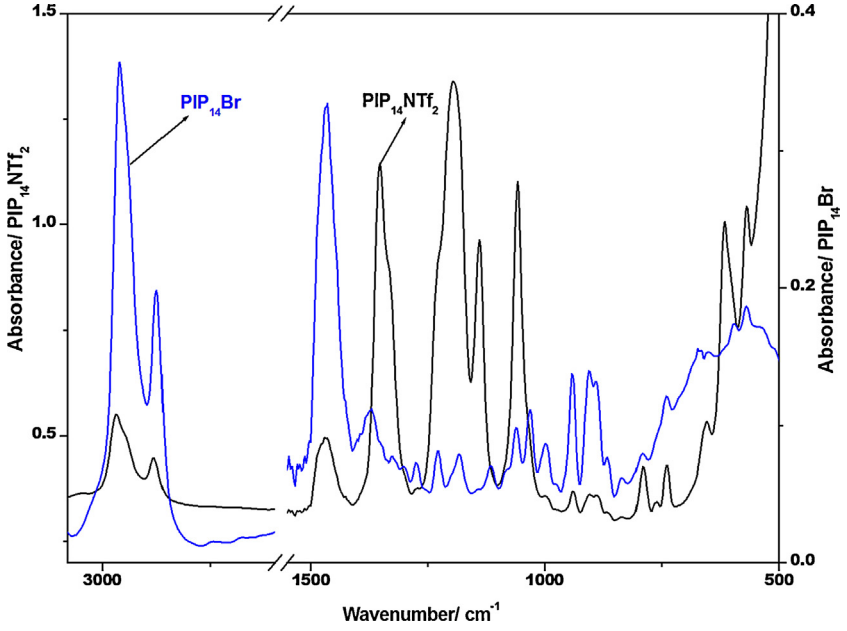

Fig. 9. Experimental IR spectra for $PIP_{14}Br$ and $PIP_{14}NTf_2$.

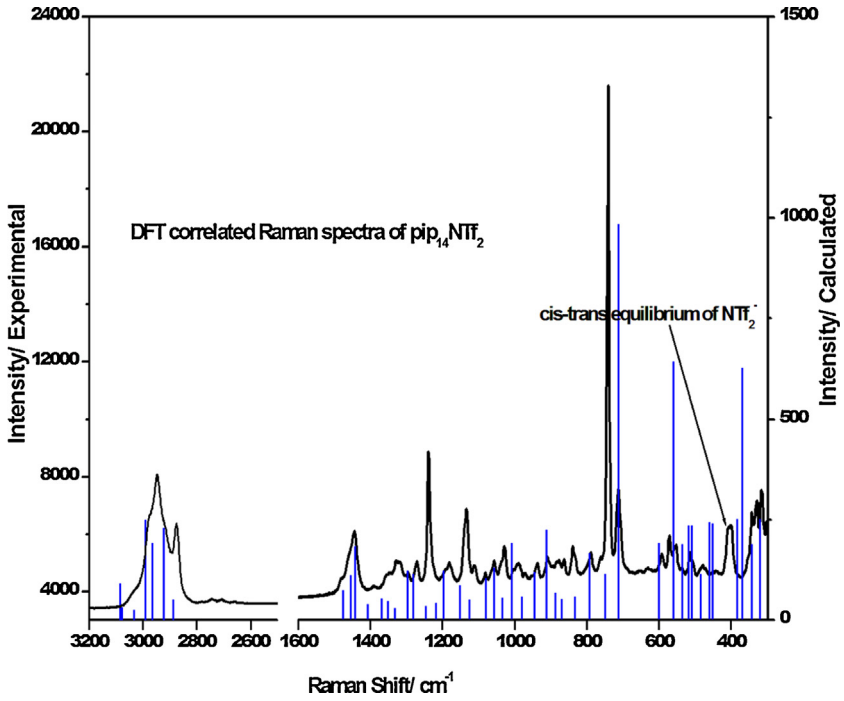

Fig. 10. Raman spectrum of neat $PIP_{14}NTf_2$ correlated with DFT calculated vibrational bands (vertical lines). A scaling factor of 0.966 was required above 1500 cm^{-1} to reproduce the experimental observations in the C—H stretch and fingerprint regions.

experimental IR spectra for $PIP_{14}Br$ and $PIP_{14}NTf_2$ are shown in Fig. 9.

Although a conformational study of cation and anion is not possible through IR, Raman spectra are found to be very helpful. The experimental and simulated Raman spectra of $PIP_{14}NTf_2$ are shown in Fig. 10. The experimental Raman spectra have been correlated with the DFT calculated Raman intensity. Raman activities obtained by Gaussian program were converted to Raman intensity using a procedure described in literatures [39–42]. The fingerprint region consists of one strong, sharp line at 740 cm^{-1}, which is characteristic for NTf_2^- anion and corresponds to S—N and C—F stretching coupled with SO_2 wagging motion. In addition, relatively less intense peaks are seen at 323, 343, 403, 714, 1081, 1135, 1237, and 1441 cm^{-1} in the fingerprint region, while a broad conglomerate of some bands appears in the 2800–3100 cm^{-1} interval. Raman spectra reported by Siqueira et al. [31] very recently for $PIP_{14}NTf_2$ is found to correspond well with our experimental and theoretical results. The majority of these peaks have been assigned based on reported values and interpreted satisfactorily on the basis of our DFT (6–31++G(d,p)) calculation (see Table 4) [46]. More specifically, the S=O symmetric and asymmetric stretching bands appear at 1081 and 1276 cm^{-1}, respectively. Sharp bands at 2874 and 2944 cm^{-1} along with a hump at 2979 cm^{-1} are also observed in the C—H stretching region. Correlation of Raman frequencies calculated using two different methods (DFT and H–F) with experimental peak positions is shown in Fig. 11. DFT calculation is found to reproduce the experimental frequencies better compared to H–F method. The Raman spectra

Table 4
Selected Raman shifts (wavenumber) of $PIP_{14}NTf_2$ (*trans*oid form) calculated at DFT and H–F methods. Some of the calculated bands are closely matching with that of experimental bands which might be just coincidental considering that the calculations were done in gas phase while Raman spectra were recorded in its normal phase of existence.

Observed ν (cm^{-1})	*Trans*oid form		Assignment of bands
	DFT ν (cm^{-1})	H–F ν (cm^{-1})	
301	294	348	Wagging in SO2 coupled with C—F sym bending
323	324	348	Twisting in SO2
343	342	377	Rocking of H—C—H in piperidinium ring
349	366	398	Rocking of SO2 and S—N stretching
396	388	447	Rocking of SO2
569	560	581	Scissoring in SO2 and F—C—F
714	701	810	S—N stretching and C—F symmetric stretching
740	755	866	S—N stretching and C—F symmetric stretching coupled with SO2 wagging
837	837	895	Wagging of H—C—H in piperidinium ring
909	912	977	C—C stretching in butyl group
1028	1060	987	N—CH3 stretching
1081	1081	1239	S=O sym stretching
1135	1152	1341	C—F stretching
1237	1196	1386	C—F sym bending in NTf_2 (umberalla bending)
1276	1285	1440	S=O asymmetric stretching
1441	1488	1606	Scissoring of H—C—H
2873	3015	3162	sym C—H stretching in butyl group
2945	3089	3241	asym C—H stretching in piperidinium ring
2980	3113	3292	sym C2—H stretching in piperidinium ring

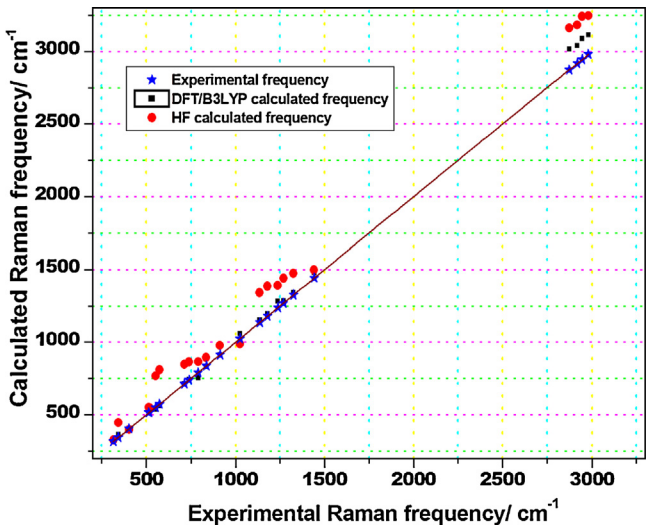

Fig. 11. Correlation diagram for Raman spectrum of $PIP_{14}NTf_2$: experimental versus calculated Raman transition frequencies. (DFT and H–F methods). Scaling factors = 0.966 (B–3L–Y–P) and 0.915 (H–F).

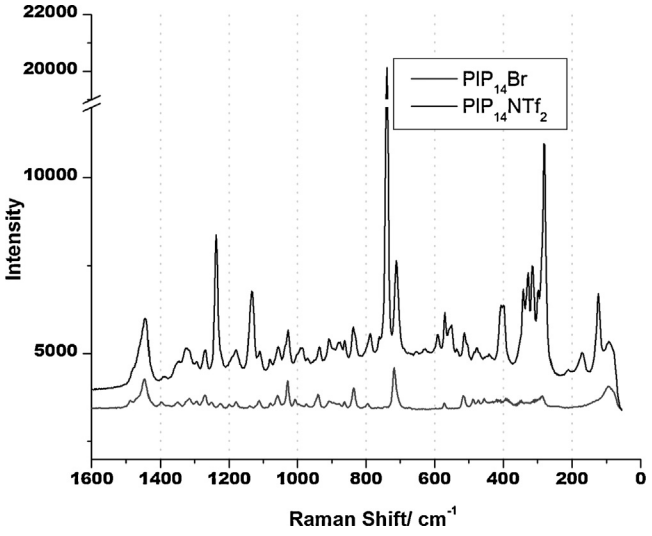

Fig. 12. Experimental Raman spectra of $PIP_{14}Br$ and $PIP_{14}NTf_2$ (fingerprint region).

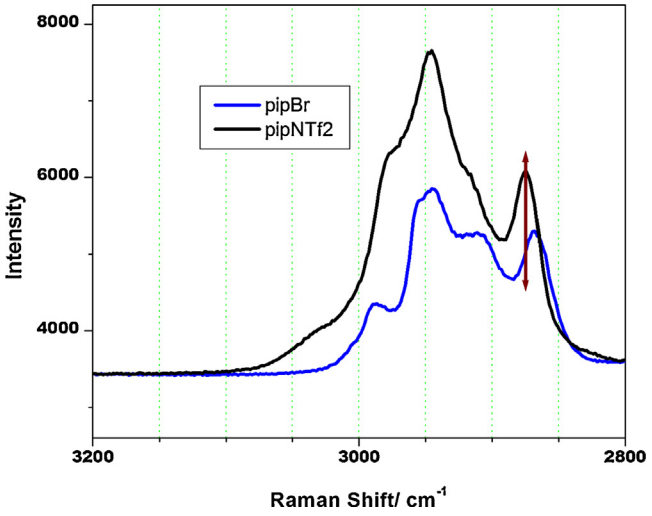

Fig. 13. Experimental Raman spectra of $PIP_{14}Br$ and $PIP_{14}NTf_2$ (C—H region).

for $PIP_{14}Br$ and $PIP_{14}NTf_2$ in the fingerprint and C—H regions are shown in Figs. 12 and 13, respectively. While insignificant shift is observed in the fingerprint region, the C—H region shows significant shifts between $PIP_{14}Br$ and $PIP_{14}NTf_2$ ILs as evident in Fig. 13. Blue shift of ($\sim$9 cm^{-1}) is observed for $PIP_{14}Br$ compared to that of $PIP_{14}NTf_2$. This vibrational spectroscopic result clearly indicates that the strength of hydrogen bond is stronger in case of $PIP_{14}Br$ when compared to $PIP_{14}NTf_2$. This result is also in agreement with our previous report for similar derivatives but with imidazolium cation [26]. Hobza and Havlas have described this blue shift solely as due to the increase in strength of hydrogen bonding between cation and anion [61]. Further, the Raman spectrum interestingly indicates a *cis–trans* equilibrium of NTf_2^-anion (shown in Fig. 10; the corresponding band is indicated by an arrow) in liquid $PIP_{14}NTf_2$. The existence of two closely spaced bands (between 380 and 450 cm^{-1}) indicates the coexistence of two conformational forms. Details of *cis*oid–*trans*oid conformations are discussed in Section 3.5.

3.5. Existence of *cis*oid–*trans*oid equilibrium of the anion in $PIP_{14}NTf_2$

The experimental Raman spectrum of $PIP_{14}NTf_2$ shown in Fig. 10 contains two closely spaced bands due to vibrational motion of NTf_2^- in the region of 380–450 cm^{-1}. To interrogate this Raman signature, we here focus on the calculated and experimental spectra below 700 cm^{-1}. Raman frequencies calculated for both *cis*oid and *trans*oid NTf_2^- anion containing PIP_{14} ILs using DFT/B3–L–Y–P/6–31 + +G(d,p) in the low-frequency region are tabulated in Table 5 and the same has also been plotted in Fig. 14a. The bands are assigned based on the literature [53] and on observing relative displacements of the atoms using GaussView program. The figure clearly depicts that some of the bands have been shifted considerably on change of conformation of NTf_2, while some have different intensities. The out-of-plane bending of N in NTf_2^- anion is observed at 207 cm^{-1} in *trans*oid conformation, while it is red shifted to 188 cm^{-1} in *cis*oid-$PIP_{14}NTf_2$. The band at 278 cm^{-1}, which is assigned to the SO_2 twisting in the *trans*oid form, is shifted to 257 cm^{-1} in the *cis*oid form. The SO_2 scissoring observed at 324 cm^{-1} in the *trans*oid form is shifted to 304 cm^{-1} in the *cis*oid form. The SO_2 rocking in the *trans*oid conformation observed at 388 cm^{-1} moves to 406 cm^{-1} in the *cis*oid conformation. The S–N–S in-plane bending observed at 602 cm^{-1} in the *trans*oid conformation is shifted to 627 cm^{-1} in the *cis*oid conformation. Other bands are found to show a maximum shift of about 10 cm^{-1}.

Fig. 14b compares the observed Raman spectrum (solid curve) with the *cis*oid (blue vertical line) and *trans*oid $PIP_{14}NTf_2$ (green vertical line) DFT-calculated frequencies in the 380–420 cm^{-1} region. This region represents Raman bands of the *cis*oid and *trans*oid conformers of NTf_2^-, as described in several literatures for imidazolium based ILs [43,53]. Further two closely spaced bands, at 617 and 651 cm^{-1}, that have been observed experimentally are identified as scissoring of S–N–S in *trans* and *cis* conformations, respectively, with the help of DFT calculation. As there is no calculated band present between 603–701 cm^{-1} for *trans*

Table 5
Important Raman bands observed in *cis*oid–*trans*oid conformation of $PIP_{14}NTf_2$ anion.

*trans*oid form	*cis*oid form	Assignment of bands
DFT ν (cm^{-1})	DFT ν (cm^{-1})	
207	188	Out of plane bending of N
278	257	Twisting of SO_2
324	304	SO_2 scissoring
388	406	Rocking of SO_2
602	627	S–N–S in plane bending

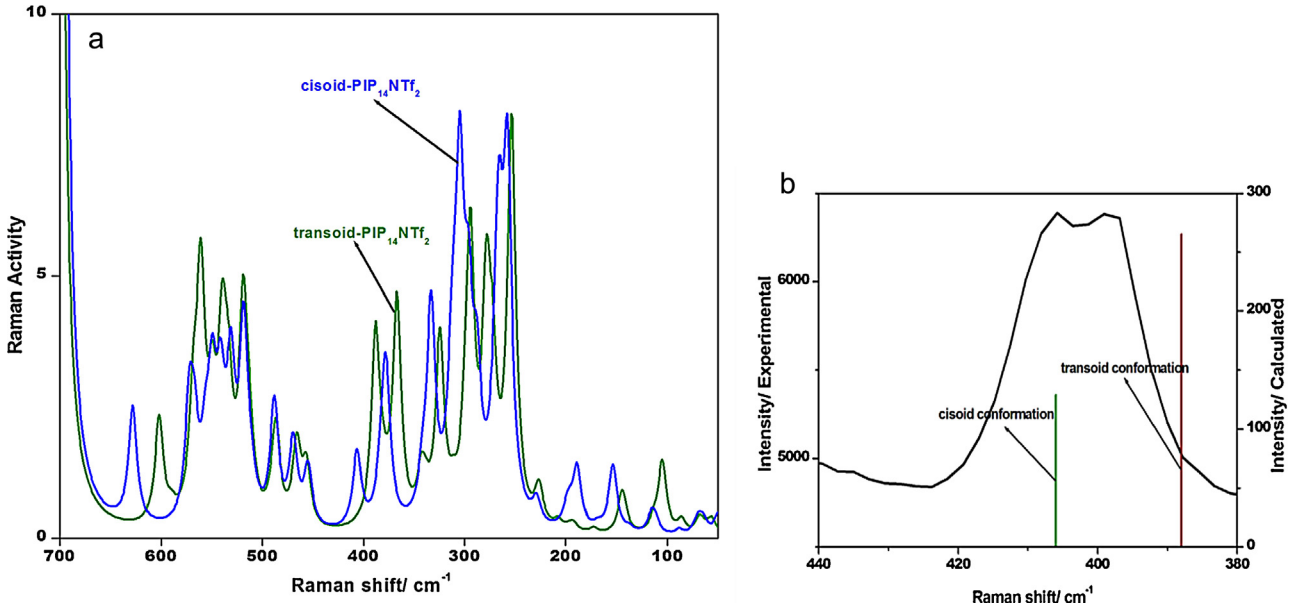

Fig. 14. (a) Correlation of DFT calculated Raman spectra of *cis*oid and *trans*oid $PIP_{14}NTf_2$. (b) Experimental Raman spectra (continuous line) correlated with DFT calculated Raman intensity (vertical line) for *cis*oid (blue line) and *trans*oid (brown line) form NTf_2 anion containing $PIP_{14}NTf_2$ in the 380–440 cm^{-1} region. For interpretation of the references to color in this figure legend, the reader is referred to the web version of this article.

conformer and one extra band is observed experimentally in this region, it can be recognized for its origin from the *cis* conformation from DFT calculation. DFT-calculated Raman bands in this region correspond to the wagging modes of SO_2 at 388 cm^{-1} for *trans*oid and 406 cm^{-1} for *cis*oid conformations. The Raman frequency calculation using DFT produces no vibrations between 389–455 cm^{-1} for *trans*oid-$PIP_{14}NTf_2$ and between 379–405 cm^{-1} for *cis*oid-$PIP_{14}NTf_2$, as clearly seen in Fig. 14a. Hence, we confirm that NTf_2^- in the liquid state of $PIP_{14}NTf_2$ consists of two conformers in equilibrium. The frequencies we obtained from DFT calculation for the SO_2 wagging is consistent with the literature available for imidazolium cation based NTf_2 ILs [43,53]. These *trans*oid and *cis*oid marker bands are reported to appear at 397 and 405 cm^{-1} for $hmimNTf_2$, almost at the same position as in $emimNTf_2$ [53].

4. Conclusions

In *N*-butyl-*N*-methylpiperidiniumbis(trifluoromethanesulfonyl) imide ($PIP_{14}NTf_2$) optimized structure, the piperidinium ring was found to exist in a chair form, which is the most stable conformation, when compared with boat and twist-boat forms. Also the butyl group was observed to be stable in *gauche* conformation with respect to the piperidinium ring. In bmimBr, no H-bonding was observed between the anion and alkyl chain. In contrast, in $PIP_{14}Br$, two H-bonding with the alkyl chain along with one H-bonding with a hydrogen on the piperidine ring was observed. Hence, this higher number of H-bonding present in $PIP_{14}Br$ is one of the main reasons to its higher melting point compared to imidazolium analog, bmimBr. The interaction energy for $PIP_{14}Br$ was estimated to be higher than that for $PIP_{14}NTf_2$, showing a positive correlation between interaction energy and melting point. DFT calculation generated the most stable geometry for $PIP_{14}NTf_2$ when compared with three different (DFT, MP2, and H–F) methods. The *trans*oid conformation of NTf_2^- anion was found to be more stable than the *cis*oid conformation by 1.04 kcal/mol. Interestingly, the experimental Raman spectrum of liquid $PIP_{14}NTf_2$ (between 380 and 450 cm^{-1}) clearly indicates the existence of *cis*oid–*trans*oid conformational equilibrium of NTf_2^-. DFT calculation predicts the Raman band arising from the SO_2 wagging to appear at 388 cm^{-1} (*trans*oid) and 406 cm^{-1} (*cis*oid). Blue shift in C—H stretching frequency has been observed for $PIP_{14}Br$ which clearly indicates stronger hydrogen bonding in $PIP_{14}Br$ compared to $PIP_{14}NTf_2$ IL. Further, the existence of rotamers of the anion in $PIP_{14}NTf_2$ might account for the drastic decrease in melting point when compared with $PIP_{14}Br$.

Acknowledgements

Financial assistance from DRDO (ARMREB/HEM/2012/140), New Delhi, India is gratefully acknowledged. Authors also thank BHU and Hyderabad Central University, Hyderabad, for providing computational facility. MLS thanks UGC for providing fellowship. SS would like to thank the Editor for constructive suggestions and Prof. D. Michalska for help and discussion regarding calculation of Raman intensities.

References

[1] J.S. Wilkes, Green Chem. 4 (2002) 73–80.
[2] R.D. Rogers, G.A. Voth, Acc. Chem. Res. 40 (2007) 1077–1078.
[3] T. Tsuda, K. Kondo, T. Tomioka, Y. Takahashi, M.S. Kuwabata, C.L. Hussey, Angew. Chem. Int. Ed. 50 (2011) 1310–1313.
[4] K. Lava, K. Binnemans, T. Cardinaels, J. Phys. Chem. B 113 (2009) 9506–9511.
[5] M. Egashira, S. Okada, J. Yamaki, Y.M.N. Morita, Electrochim. Acta 50 (2005) 3708–3712.
[6] A. Triolo, O. Russina, B. Fazio, G.B. Appetecchi, M. Carewska, S. Passerini, J. Chem. Phys. 130 (2009) 164521–164526.
[7] J. Salminen, N. Papaiconomou, R.A. Kumara, J.M. Lee, J. Kerr, J. Newmana, J.M. Prausnitz, Fluid Phase Equilib. 261 (2007) 421–426.
[8] L.X. Yuan, J.K. Feng, X.P. Ai, Y.L. Cao, S.L. Chen, H.X. Yang, Electrochem. Commun. 8 (2006) 610–614.
[9] K. Matsumoto, R. Hagiwara, Inorg. Chem. 48 (2009) 7350–7358.
[10] C.J. Rao, R.V. Krishnan, K.A. Venkatesan, K. Nagarajan, T.G. Srinivasan, J. Therm. Anal. Calorim. 97 (2009) 937–943.
[11] A. Lewandowski, A. Swiderska, Solid State Ionics 169 (2004) 21–24.
[12] H. Sakaebe, H. Matsumoto, Electrochem. Commun. 5 (2003) 594–598.
[13] F.F.C. Bazito, Y. Kawano, R.M. Torresi, Electrochim. Acta 52 (2007) 6427–6437.
[14] Z.B. Zhou, H. Matsumoto, K. Tatsumi, Chem. Eur. J. 12 (2006) 2196–2212.
[15] Y.U. Paulechka, G.J. Kabo, V.N. Emel'yanenko, J. Phys. Chem. B 112 (2008) 15708–15717.
[16] T.Y. Cho, S.G. Yoon, S.S. Sekhon, C.H. Han, Bull. Korean Chem. Soc. 32 (2011) 2058–2062.
[17] W.M. Reichert, W.A. Henderson, P.C. Trulove, J.J. Urban, H.C. De Long, ECS Trans. 33 (2010) 667–677.

[18] B. Haddad, D. Villemin, E. Belarbi, J. Mater. Environ. Sci. 3 (2012) 312–319.
[19] P. Wasserscheid, T. Welton, Ionic Liquids Synthesis, 2nd Ed., VCH-Wiley, Weinheim, 2007.
[20] R.D. Rogers, K.R. Seddon, Science 302 (2003) 792–793.
[21] F. Endres, S.Z.E. Abedin, Phys. Chem. Chem. Phys. 8 (2006) 2101–2116.
[22] K. Iwata, H. Okajima, S. Saha, H. Hamaguchi, Acc. Chem. Res. 40 (2007) 1174–1181.
[23] S. Shigeto, H. Hamaguchi, Chem. Phys. Lett. 427 (2006) 329–332.
[24] S. Patra, A. Samanta, J. Phys. Chem. B 116 (2012) 12275–12283.
[25] H. Wang, J. Wang, L. Zhang, Vib. Spectrosc. 68 (2013) 20–28.
[26] M. Shukla, N. Srivastava, S. Saha, J. Mol. Struct. 975 (2010) 349–356.
[27] M. Shukla, N. Srivastava, S. Saha, Ionic Liq.-Classes Prop. (2011) 150–170.
[28] H.C. Chang, J.C. Jiang, C.Y. Chang, J.C. Su, C.H. Hung, Y.C. Liou, S.H. Lin, J. Phys. Chem. B 112 (2008) 4351–4356.
[29] K. Fumino, R. Ludwig, J. Mol. Liq. 192 (2014) 94–102.
[30] V. Kempter, B. Kirchner, J. Mol. Struct. 972 (2010) 22–34.
[31] L.J.A. Siqueira, V.R.L. Constantino, F.F. Camilo, R.M. Torresi, M.L.A. Temperini, M. C.C. Ribeiro, C.M.S. Izumi, Spectrochim. Acta Part A: Mol. Biomol. Spectrosc. 122 (2014) 469–475.
[32] H.N.N. Venkata, N. Nomura, S. Shigeto, J. Raman Spectrosc. 42 (2011) 1913–1915.
[33] M.J. Frisch, G.W. Trucks, H.B. Schlegel, G.E. Scuseria, M.A. Robb, J.R. Cheeseman, J.A. Montgomery, T. Vreven, K.N. Kudin, J.C. Burant, J.M. Millam, S.S. Iyengar, J. Tomasi, V. Barone, B. Mennucci, M. Cossi, G. Scalmani, N. Rega, G.A. Petersson, H. Nakatsuji, M. Hada, M. Ehara, K. Toyota, R. Fukuda, J. Hasegawa, M. Ishida, T. Nakajima, Y. Honda, O. Kitao, H. Nakai, M. Klene, X. Li, J.E. Knox, H.P. Hratchian, J.B. Cross, V. Bakken, C. Adamo, J. Jaramillo, R. Gomperts, R.E. Stratmann, O. Yazyev, A.J. Austin, R. Cammi, C. Pomelli, J.W. Ochterski, P.Y. Ayala, K. Morokuma, G.A. Voth, P. Salvador, J.J. Dannenberg, V.G. Zakrzewski, S. Dapprich, A.D. Daniels, M.C. Strain, O. Farkas, D.K. Malick, A.D. Rabuck, K. Raghavachari, J.B. Foresman, J.V. Ortiz, Q. Cui, A.G. Baboul, S. Clifford, J. Cioslowski, B.B. Stefanov, G. Liu, A. Liashenko, P. Piskorz, I. Komaromi, R.L. Martin, D.J. Fox, T. Keith, M.A. Al-Laham, C.Y. Peng, A. Nanayakkara, M. Challacombe, P.M.W. Gill, B. Johnson, W. Chen, M.W. Wong, C. Gonzalez, J.A. Pople, Gaussian 03, Revision D.02, Gaussian Inc., Wallingford, CT, 2004.
[34] W. Kohn, L.J. Sham, Phys. Rev. B 140 (1965) 1133–1138.
[35] C. Lee, W. Yang, R.G. Parr, Phys. Rev. B 37 (1988) 785–789.
[36] A.D. Becke, J. Chem. Phys. 98 (1993) 5648–5652.
[37] E.R. Talaty, S. Raja, V.J. Storhaug, A. Dolle, W.R. Carper, J. Phys. Chem. B 108 (2004) 13177–13184.
[38] R. Dennington, T. Keith, J. Millam, Semichem Inc. Shawnee Mission, KS, GaussView, Version 5, 2009.
[39] P.L. Polavarapu, J. Phys. Chem. 94 (1990) 8106.
[40] G. Keresztury, S. Holly, G. Besenyei, J. Varga, A.Y. Wang, J.R. Durig, Spectrochim. Acta Part A 49 (1993) 2007–2026.
[41] H.A. Witek, K. Morokuma, A. Stradomska, J. Chem. Phys. 121 (2004) 5171.
[42] D. Michalska, R. Wysokinski, Chem. Phys. Lett. 403 (2005) 211–217.
[43] K. Fujii, T. Fujimori, T. Takamuku, R. Kanzaki, Y. Umebayashi, S. Ishiguro, J. Phys. Chem. B 110 (2006) 8179–8183.
[44] Y. Umebayashi, T. Mitsugi, S. Fukuda, T. Fujimori, K. Fujii, R. Kanzaki, M. Takeuchi, S. Ishiguro, J. Phys. Chem. B 111 (2007) 13028–13032.
[45] K. Fujii, S. Seki, S. Fukuda, R. Kanzaki, T. Takamuku, Y. Umebayashi, S. Ishiguro, J. Phys. Chem. B 111 (2007) 12829–12833.
[46] A.V. Blokhin, Y.U. Paulechka, A.A. Strechan, G.J. Kabo, J. Phys. Chem. B 112 (2008) 4357–4364.
[47] A.P. Scott, L. Radom, J. Phys. Chem. 100 (1996) 16502–16513.
[48] R. Arnaud, D. Benrabah, J.Y. Sanchez, J. Phys. Chem. 100 (1996) 10882–10891.
[49] P. Johansson, S.P. Gejji, J. Tegenfeldt, J. Lindgren, Electrochim. Acta 43 (1998) 1375–1379.
[50] J.N.C. Lopes, A.A.H. Padua, J. Phys. Chem. B 108 (2004) 16893–16898.
[51] C.M. Forsyth, D.R. MacFarlane, J.J. Golding, J. Huang, J. Sun, M. Forsyth, Chem. Mater. 14 (2002) 2103–2108.
[52] L.F.O. Faria, J.R. Matos, M.C.C. Ribeiro, J. Phys. Chem. B 116 (2012) 9238–9245.
[53] A.M. Moschovi, S. Ntais, V. Dracopoulos, V. Nikolakis, Vib. Spectrosc. 63 (2012) 350–359.
[54] A. Bondi, J. Phys. Chem. B 68 (1964) 441–451.
[55] S. Saha, S. Hayashi, A. Kobayashi, H. Hamaguchi, Chem. Lett. 32 (2003) 740–741.
[56] S. Saha, H. Hamaguchi, J. Phys. Chem. B 110 (2006) 2777–2781.
[57] Y. Wang, H. Li, S. Han, J. Chem. Phys. 123 (2005) 174501.
[58] J.M. Lee, J. Chem. Eng. 172 (2011) 1066–1071.
[59] F.F.C. Bazito, Y. Kawano, R.M. Torresi, Electrochim. Acta 52 (2007) 6427–6437.
[60] W. Li, C. Qi, H. Rong, X. Wu, L. Gong, Chem. Phys. Lett. 542 (2012) 26–32.
[61] P. Hobza, Z. Havlas, Chem. Rev. 100 (2000) 4253–4264.